Quantifying hard coal mines CH_4 emissions from TROPOMI and IASI observations using high-resolution CAMS forecast data and the wind-assigned anomaly method

Qiansi Tu[1,2], Matthias Schneider[2], Frank Hase[2], Farahnaz Khosrawi[2], Benjamin Ertl[2,3], Jaroslaw Necki[4], Darko Dubravica[2], Christopher J. Diekmann[2], Thomas Blumenstock[2], Dianjun Fang[1,5]

[1]School of Mechanical Engineering, Tongji University, Shanghai, China
[2] Karlsruhe Institute of Technology (KIT), Institute of Meteorology and Climate Research (IMK-ASF), Karlsruhe, Germany
[3] Karlsruhe Institute of Technology, Steinbuch Centre for Computing (SCC), Karlsruhe, Germany
[4]AGH – University of Science and Technology, Krakow, Poland
[5]Qingdao Sino-German Institute of Intelligent Technologies, Qingdao, China

Correspondence to: Qiansi Tu (qiansi.tu@kit.edu), Matthias Schneider (matthias.schneider@kit.edu)

Abstract. Intensive coal mining activities in the Upper Silesian Coal Basin (USCB) in southern Poland are resulting in large amounts of methane (CH_4) emissions. Annual CH_4 emission reached 448 kt according to the European Pollutant Release and Transfer Register (E-PRTR, 2017). As a CH_4 emission hot spot in Europe, it is of importance to investigate its emission sources and make accurate emission estimates.

In this study, we use satellite-based total column-averaged dry-air mole fraction of CH_4 (XCH_4) from the TROPOspheric Monitoring Instrument (TROPOMI) and tropospheric XCH_4 ($TXCH_4$) from the Infrared Atmospheric Sounding Interferometer (IASI). In addition, the high-resolution model forecast XCH_4 and $TXCH_4$ from the Copernicus Atmosphere Monitoring Service (CAMS) are used to estimate the CH_4 emission rate averaged over three years (November 2017 to December 2020) in the USCB region (49.3° - 50.8° N and 18° - 20° E). Using the CAMS inventory (CAMS-GLOB-ANT) as the a priori knowledge (location and the proportion of the emission rate for each source in the total emissions) of the sources, together with ERA5 wind at 330 m, the wind-assigned XCH_4 anomalies for two opposite wind directions are calculated, which yields an estimated CH_4 emission of 815 ± 13 kt/year (9.7E26 ± 1.5E25 molec./s) for CAMS XCH_4 and 798 ± 11 kt/year (9.5E26 ± 1.3E25 molec./s) for CAMS $TXCH_4$. These values are very close to the total emission of the CAMS-GLOB-ANT (815 kt/year). Very good agreements between CAMS and the wind-assigned model results (R^2=0.85 for XCH_4 and $TXCH_4$) indicate that our wind-assigned method is quite robust. The similar estimates of XCH_4 and $TXCH_4$ also imply that for a strong source, the dynamically induced variations of the CH_4 mixing ratio in the upper troposphere and lower stratosphere region are of secondary importance.

This wind-assigned method is further applied to the TROPOMI XCH_4 and TROPOMI+IASI $TXCH_4$ with using the Carbon dioxide and Methane (CoMet) inventory derived for the year 2018. The calculated averaged total CH_4 emission over the USCB region is about 479 ± 4 kt/year (5.7E26 ± 4.9E24 molec./s) for TROPOMI XCH_4 and 437 ± 18 kt/year (5.2E26 ± 2.2E25

molec./s) for TROPOMI+IASI TXCH$_4$. These values are very close to the ones given in the E-PRTR inventory (448 kt/year) and the ones in the CoMet inventory (555 kt/year) and are thus in agreement with these inventories.

Since the wind speed is increasing with altitude, sensitivity tests show that higher CH$_4$ emission strengths are yielded with increasing altitude and vice versa. About 23% lower and 13% higher emission estimates are obtained when instead of the wind information at 330 m, the wind information at a lower altitude (10 m) and at a higher altitude (500 m) is used, respectively. When using different wind coverage and different wind segmentation, the estimated emission strengths change by 13.4% and -5.2%, respectively. These results suggest that our wind-assigned method is quite robust and might also serve as a simple method to estimate CH$_4$ or CO$_2$ emissions for other regions.

1 Introduction

Atmospheric methane (CH$_4$) is the second most important anthropogenic greenhouse gas (GHG) with a larger global warming potential than carbon dioxide (CO$_2$) (IPCC, 2014). The globally averaged amount of atmospheric CH$_4$ has increased by 260% to 1877 ± 2 ppb from the preindustrial era until 2019 (World Meteorological Organization, 2020). Methane sources induced by anthropogenic activities include fossil fuel production and use (e.g., coal mining, gas/oil extraction), waste disposal, and agriculture, which in total accounts for about 60% of the total CH$_4$ emissions (Saunois et al., 2020). Although most sources and sinks of CH$_4$ have been characterized, their spatial-temporal variations and relative contributions to the atmospheric CH$_4$ level are still highly uncertain (Kirschke et al., 2013; Saunois et al., 2020).

Approximately 33% of the CH$_4$ emissions from coal mining (42,000 kt/year) are estimated to come from the total fossil-fuel-related emissions during 2008-2017 (Saunois et al., 2020). CH$_4$ is released primarily to the atmosphere via ventilation shafts located at the surface during the production and processing of the coal (Saunois et al., 2020; Andersen et al. 2021). The largest contribution of CH$_4$ emission related with the coal mining activities in Europe is from southern Poland—the Upper Silesian Coal Basin (USCB) (Luther et al., 2019; Krautwurst et al., 2021). The USCB is in the Silesian Upland, which is a plateau between 200 and 300 m above sea level with a predominant south-west wind. The USCB within Poland covers an area of over 5800 km^2, and to its south is the Tatra Mountain ridge with elevations larger than 2000 m a.s.l. The European Pollutant Release and Transfer Register (E-PRTR, 2017; https://prtr.eea.europa.eu/, last access: 25 October 2021) reports that the total CH$_4$ emissions from the USCB region amount to 448 kt/year. Most of these emissions are from mining activities and heavy industry (Kostinek et al., 2021), which makes this region a hot spot of CH$_4$ emission in Europe.

To investigate the CH$_4$ emission from this hot spot, the Carbon Dioxide and Methane (CoMet) campaign was performed, covering roughly 3 weeks from May to June 2018. A variety of state-of-art instruments, including in situ and remote sensing instruments on the ground and aboard five research aircraft, were deployed in order to provide independent observations of GHG emissions on local to regional scale and provide data for satellite validation (more details can be found in Luther et al., 2019; Fiehn et al., 2020; Kostinek et al., 2021; Krautwurst et al., 2021). Many studies present similar CH$_4$ emission estimates for the region based on different instruments and methods. Luther et al. (2019) estimated CH$_4$ emissions ranging from 6 ± 1

kt/year for a single shaft to up to 109 ± 33 kt/year for a subregion of the USCB covering several shafts, by using several portable Fourier Transform Infrared (FTIR) spectrometers (Bruker EM27/SUN). Fiehn et al (2020) analyzed aircraft- and ground-based in situ observations and reported an emission estimate of 436 ± 115 kt/year and 477 ± 101 kt/year from two selected flights. An advanced model approach was introduced by Kostinek et al. (2021) to investigate two research flights in the morning and afternoon, resulting in estimated CH_4 emissions of 451 ± 77 kt/year and 423 ± 79 kt/year, respectively. Another emission estimate based on the observations from the nadir-looking passive remote sensing Methane Airborne MAPper (MAMAP) instrument accounted for 8.8 kt/year to 78.8 kt/year for a sub-clusters of ventilation shafts (Krautwurst et al., 2021). A recent study (Luther et al., 2021) displays a larger emission rate of 414 – 790 kt/year based on a network of four portable FTS instruments (EM27/SUN) during the CoMet campaign.

Launched in October 2017, the TROPOspheric Monitoring Instrument (TROPOMI) on board the Sentinel-5 Precursor satellite provides an unprecedent high spatial resolution (5.5 × 7 km^2) of the CH_4 total column-averaged dry-air mole fraction (XCH_4) (Veefkind et al., 2012; Lorente et al., 2021). An a posteriori method has been developed by Schneider et al. (2021) to obtain tropospheric XCH_4 ($TXCH_4$) by combining observations from TROPOMI and the Infrared Atmospheric Sounding Interferometer (IASI). This synergetic product is not influenced by the changing tropopause height, and it offers improved sensitivity to the tropospheric variations than the total column XCH_4 data from either sensor. The improved real-time forecast data with high resolution (0.1° × 0.1°~9 km × 9km) are produced by the Copernicus Atmosphere Monitoring Service (CAMS) (Agustí-Panareda et al., 2019; Barré et al., 2021). All data sets provide a large spatial coverage and long-term XCH_4/$TXCH_4$ observations, which help to better estimate CH_4 emission in the USCB region.

In Sect. 2 we present the data sets and methodology used in this study to derive estimated CH_4 emissions. The results and discussions are presented in Sect. 3. We present a novel wind-assigned method introduced by Tu et al., 2022, which is firstly verified by the CAMS model forecasts and then applied to the TROPOMI XCH_4 and TROPOMI+IASI $TXCH_4$ data to estimate the CH_4 emissions in the USCB region for the time period from November 2017 to December 2020, together with an uncertainty analysis. Finally, the summary and conclusions are given in Sect. 4.

2 Data sets and method

There are over 50 active ventilation shafts in the USCB region (49.3° - 50.8° N and 18° - 20° E), Poland, whose emission rates range between 0.17 kt/year and 41.02 kt/year (Gałkowski et al., 2021) (Figure 4b). Most of them are located near Katowice and further west and southwest of Katowice.

2.1 CAMS CH_4 forecast and emission inventories

The Integrated Forecasting System (IFS, https://www.ecmwf.int/en/publications/ifs-documentation, last access: 27 October, 2021) from the European Centre for Medium-Range Weather Forecasts (ECMWF) is used in the CAMS atmospheric composition analysis and forecasts system to simulate five-day CO_2 and CH_4 forecasts (Agustí-Panareda et al., 2019, Barré et

al., 2021), as well as other chemical species and aerosols (Flemming et al., 2015; Morcrette et al., 2009). This model is also used in the operational Numerical Weather Prediction (NWP) system, but with additional modules (Agustí-Panareda et al., 2019). The forecast data used in this study is the same suit as the one used in Barré et al. (2021), where the Cycle 45r1 IFS model cycle was implemented. The CAMS GHGs operational dataset includes analysis and forecast data at medium and high resolution with 137 model levels from the surface to 0.01 hPa (Barré et al., 2021). In this study we will focus on using the high-resolution CH_4 forecasts, which have a spatial resolution of 0.1° × 0.1° and a temporal resolution of 3h, starting from 00:00 UTC. Here we use the daily averaged CAMS forecasts during 9:00 UTC - 18:00 UTC at each resolution grid point. The corresponding standard deviation (STD) is considered as the noise/error.

The anthropogenic methane emissions used in the global CAMS forecasts are from the CAMS global anthropogenic emission inventory (CAMS-GLOB-ANT, Granier et al., 2019; https://permalink.aeris-data.fr/CAMS-GLOB-ANT, last access: 27 October, 2021). The CAMS-GLOB-ANT inventory is based on the emissions provided by the EDGARv4.3.2 inventory for the time period 2000-2012 (Crippa et al., 2018) and linearly extrapolated to 2020 using the trends from the CEDA global inventory for the time period 2011-2014 (Hoesly et al., 2018). The latest version (CAMS-GLOB-ANT v4.2) was released in March 2020, using the same set-up as v4.1 except for adding the emissions in 2020. The anthropogenic sources in the standard v4.2 are divided into 12 sectors and the agriculture sections are split into three sectors, including livestock, soils and waste burning (https://eccad3.sedoo.fr/, last access: 27 October, 2021). The inventory is provided as monthly mean with the same spatial resolution (0.1° × 0.1°) as the CAMS forecast data (Granier et al., 2019).

The monthly averages of the CAMS global anthropogenic emissions for different sectors in the study area of USCB are presented in Figure 1. The emissions from the sectors “agriculture soils” and “solvents” are zeros. The CH_4 emitted from ships has 19 orders of magnitude, which are much lower than the other sectors. Thus, these three sectors are not shown here. The sources from agriculture livestock (1.7E25 ± 4.0E25 molec./s) amount only 4% of the total emissions in this region. The dominant CH_4 sources in this region are fugitive sources from energy production and distribution (e.g. fuel use). With a mean value of 7.9E26 molec./s and a standard deviation of 2.2E25 molec./s, they account for 82% of the anthropogenic CH_4 emissions in the CAMS-GLOB-ANT inventory (9.7E26 molec./s in total). This becomes particularly visible in the spatially overlapping distribution within the USCB (see Figure 2). The seasonal emission variations of the fugitive sector are minor and can be ignored. Therefore, we apply the three-year mean of total emissions at grids with significant emissions without considering seasonal variations in the simple plume model (see Sect. 2.3). The total emissions amount to 9.7E26 molec./s over this study area.

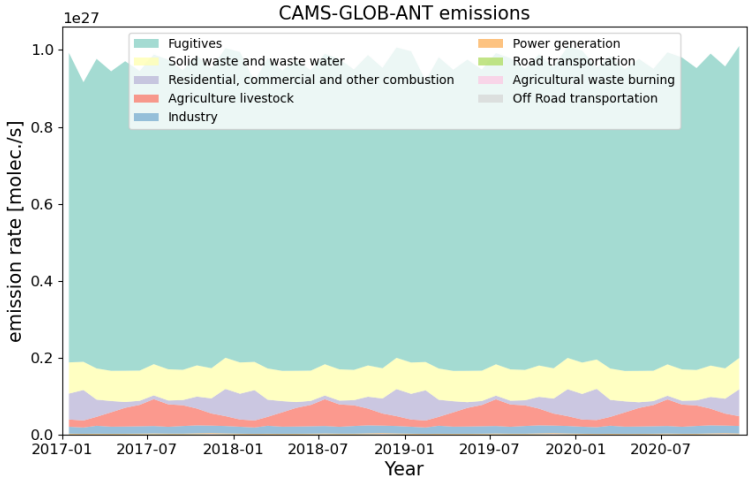

Figure 1: Stacked area plot for different sectors of the monthly averaged CAMS global anthropogenic emissions (>1E20 molec./s) in the USCB region for 2017-2020 (https://permalink.aeris-data.fr/CAMS-GLOB-ANT, last access: 22 December 2021. Granier et al., 2019).

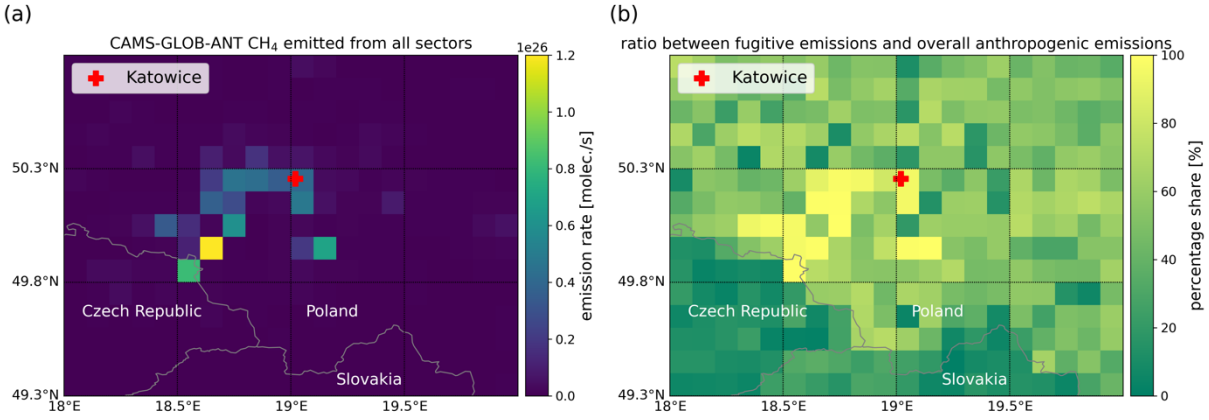

Figure 2: Spatial distribution of (a) the CAMS global anthropogenic emissions from all sectors and (b) percentage share of the fugitive emissions compared to the overall anthropogenic emissions over the USCB region on a 0.1° × 0.1° latitude/longitude grid. The fugitives are the dominant CH_4 sources.

2.2 TROPOMI and IASI data sets

The TROPOMI instrument is a nadir-viewing, imaging spectrometer, which uses passive remote sensing techniques to perform measurements of the solar radiation reflected by and radiated from the earth in the ultraviolet, the visible, the near-infrared and the shortwave infrared spectral bands (Veefkind et al., 2012). The instrument crosses the equator at about 13:30 local solar time at each orbit with a repeat cycle of 17 days. It observes a full swath (2600 km) per second with an orbit duration of 100 min. The algorithm for CH_4 column retrieval is called RemoTeC algorithm and it has been extensively used to derive CO_2 and

CH_4 retrievals from the Greenhouse Gases Observing Satellite (GOSAT) and Orbiting Carbon Observatory-2 (OCO-2; Boesch et al., 2011; Butz et al., 2009, 2011; Hasekamp and Butz, 2008; Schepers et al., 2012). An updated retrieval algorithm has been implemented by Lorente et al. (2021) to obtain a data suit with less scatter and a higher resolution surface altitude database. This updated TROPOMI XCH_4 dataset has been validated with the Total Carbon Column Observing Network (TCCON) (-3.4 ± 5.6 ppb) and GOSAT (-10.3 ± 16.8 ppb), showing very good agreements. In this study the TROPOMI XCH_4 during November 2017 and December 2020 within the study area over the USCB region is investigated. The data provided by Lorente et al. (2021) includes an additional quality filter parameter (quality value, qa). TROPOMI XCH_4 with qa=1.0 represents the data under clear-sky and low-cloud atmospheric conditions and the problematic data points are removed as well. This quality filter has been applied in this study and about 16,000 data are derived over the three-year time period considered in this study.

The IASI instrument is a nadir viewing Fourier-transform spectrometer that measures the infrared part of the electromagnetic spectrum. IASI measurements are performed with a horizontal resolution of 12 km and a full swath width of about 2200 km on the ground. It is the key payload element of the polar-orbiting Metop-A -B and -C satellites. These satellites overpass the equator at 09:30 in the morning and 21:30 local time in the evening with about 14 orbits per day. It provides unprecedented accurate vertical information of atmospheric temperature and humidity, which helps to improve numerical weather prediction (NWP) (Collard, 2007; Coopmann et al., 2020). The thermal infrared nadir spectra of IASI have been successfully used in retrieving different atmospheric trace gas profiles and these retrievals are especially sensitive between the middle troposphere and the stratosphere (García et al., 2018; Diekmann et al., 2021; Schneider et al., 2021, 2022). By combining the IASI CH_4 profiles and the TROPOMI CH_4 total column, which has a higher sensitivity near ground, we are able to detect the tropospheric XCH_4 ($TXCH_4$) independently from CH_4 at higher altitudes. The combined product cannot be obtained by either the TROPOMI or IASI product independently. The combined product shows a weak positive bias of about 1 % with respect to the reference data (Schneider et al., 2021). We refer to this product in the following as the TROPOMI+IASI $TXCH_4$ and it comprises about 12,000 data points for the time period considered in this study.

2.3 Simple plume model and wind-assigned anomaly method

The averaged distribution of emitted CH_4 over a long-term period can be modeled simply as an evenly-distributed cone-shape dispersion based on the wind and source strength. Since CH_4 is a long-lived gas, its decay is negligible for short periods and not considered in the model. This model is referred to as simple cone plume model (see Figure A- 1). This model is easy to apply, and the estimated emission strengths are reasonable compared with the ones from other studies (Tu et al., 2022).

Based on the simple plume model, the enhanced CH_4 column (ΔCH_4) at the downwind side of the location (x_i, y_i) is computed as:

$$\Delta CH_{4\,(x_i,y_i)} = \frac{\varepsilon}{v \cdot d_{(xi,yi)} \cdot \alpha} \qquad \textbf{Eq. 1}$$

where the emission strength ε is the a priori knowledge from the CAMS-GLOB-ANT data set or from the coal mine ventilation shafts in this study (see Sect. 3.2). Their emission rates are assumed to be constant with time from 2017 to 2020. α is the angle

of the emission cone and has an empirical value of 60°, which has been derived from TROPOMI NO_2 measurements (Tu et al., 2022). v is the wind speed from ERA5, which is the fifth generation ECMWF reanalysis product using 4D-Var data assimilation and model forecasts in Cycle 41R2 of the ECMWF IFS model (Copernicus Climate Change Service, C3S, 2017, Hersbach et al., 2020). ERA5 provides hourly estimates on 137 pressure levels in the vertical covering the atmosphere from the surface up to 0.01 hPa, with a spatial resolution of 0.25º×0.25º (Hersbach et al., 2020). d is the distance between the downwind location and the CH_4 emission source. Each individual source either from the CAMS-GLOB-ANT inventory or from the knowledge of the ventilation shafts is considered as an individual point source. The daily plume from each point source (location at (i,j)) is averaged over daytime (8:00 UTC - 18:00 UTC):

$$\overline{\mathrm{XCH_4}}_{(i,j)} = \frac{1}{11}\sum_{t=1}^{11} \mathrm{XCH_4}_{(i,j),t} \quad \textbf{Eq. 2}$$

these daily plumes are super-positioned over all point sources to obtain a daily plume ($\overline{\mathrm{XCH_4}}_{\mathrm{daily}}$):

$$\overline{\mathrm{XCH_4}}_{\mathrm{daily}} = \sum_{s=1}^{N_s} \overline{\mathrm{XCH_4}}_{(i,j),s} \quad \textbf{Eq. 3}$$

where N_s represents the number of the sources.

The wind distributions at different height levels (10 m, ~330 m, ~500 m) over the USCB region are presented in Figure 3. The wind speed increases with increasing altitude (see **Table 1**). The ERA5 wind is divided into two opposite wind regimes based on directions (e.g., 135°-315° for SW and the rest for NE). For each wind regime sector, an averaged plume is computed:

$$\overline{\mathrm{XCH_4}}_{\mathrm{SW/NE}} = \frac{1}{N_d}\sum_{d=1}^{N_d} \overline{\mathrm{XCH_4}}_{\mathrm{daily,d}} \quad \textbf{Eq. 4}$$

where N_d is the number of the days with SW wind or NE wind.

The difference of the two plumes is therefore the wind-assigned anomaly:

$$\mathrm{wind-assigned\ anomaly} = \overline{\mathrm{XCH_4}}_{\mathrm{NE}} - \overline{\mathrm{XCH_4}}_{\mathrm{SW}} \quad \textbf{Eq. 5}$$

The estimated emission strengths can be calculated by fitting the modelled anomalies to the known anomalies from e.g. CAMS XCH_4/$TXCH_4$, and TROPOMI and TROPOMI+IASI observations. Note that CH_4 has a lifetime of around 12 years, which results in a high background concentration compared to the newly emitted CH_4. Thus, the contributions from the background should be removed for correctly estimating emissions (Liu et al., 2021). The background is considered to consist of a constant value, a linear increase with time, a seasonal cycle, a daily anomaly and a horizontal anomaly. For more details, see the Appendix in Tu et al., 2022.

This method was firstly used to estimate the CH_4 emission from landfills in Madrid, Spain based on nearly three-year space-borne XCH_4 data, and different opening angles were investigated to obtain an empirical value (60º) (Tu et al., 2022). The CH_4 emission strengths derived from satellite products have the same orders of magnitude as the ones from single-day observations by ground-based instruments, showing that this method works properly.

Table 1: Number of days and the averaged wind speed (± standard deviation) per specific wind area during daytime (08:00 UTC – 18:00 UTC) at different vertical levels from November 2017 to December 2020 over the USCB region. The days for the three-year average coincide with the TROPOMI overpass days.

	NE / >315° or <135°		SW / 135° – 315°	
	Number of days in total (%)	**Averaged wind speed ± standard deviation (m s^{-1})**	**Number of days in total (%)**	**Averaged wind speed ± standard deviation (m s^{-1})**
10 m	39.1	3.2 ± 1.5	56. 9	3.4 ± 1.6
~330 m (975 hPa)	38.7	4.1 ± 2.2	56.9	4.3 ± 2.3
~500 m (950 hPa)	38.7	5.0 ± 2.7	57.3	5.9 ± 3.5

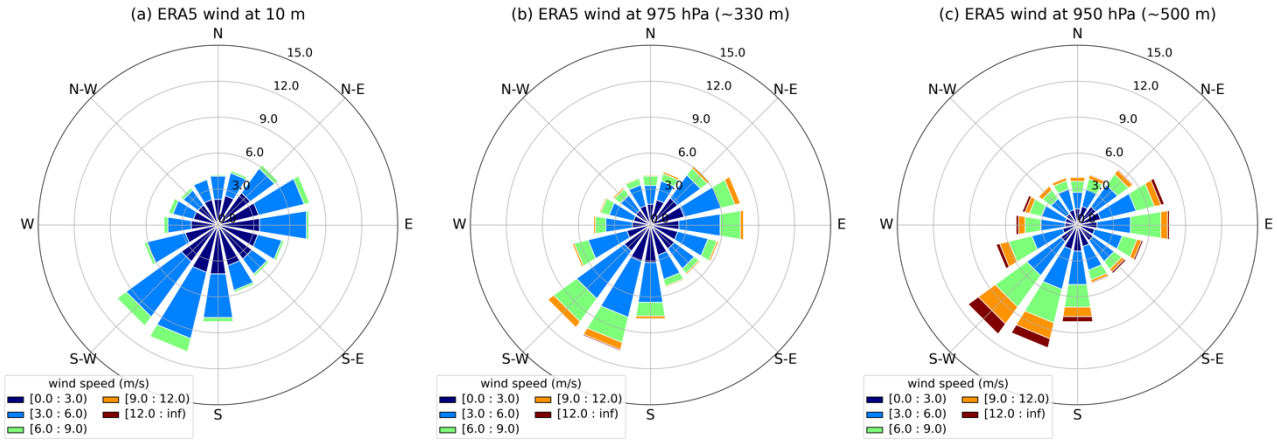

Figure 3: Windrose plots for daytime (08:00 UTC – 18:00 UTC) from November 2017 to December 2020 for the ERA5 model wind at different vertical levels (10 m, ~330 m and ~500 m). The days for the three-year average coincide with the TROPOMI overpass days.

3. Results and discussion

3.1 Estimated emissions derived from CAMS forecasts (evaluation of the method)

The CAMS forecast XCH_4 data from November 2017 to December 2020 within the study area are illustrated in Figure 4 left. The areas with high XCH_4 amounts fit well with the CAMS anthropogenic CH_4 emissions (square symbols). Similar to the CoMet inventory, high sources in the CAMS-GLOB-ANT inventory are centered in this region, but there are other weaker sources outside. The total emission rate of the CoMet inventory is 555 kt/year (6.6E26 molec./s), which is slightly less than the CAMS-GLOB-ANT emissions (815 kt/year). This is probably because the CAMS-GLOB-ANT includes more CH_4 emission sources, e.g., wastes, and combustion from residential, commercial, which account to about 20%.

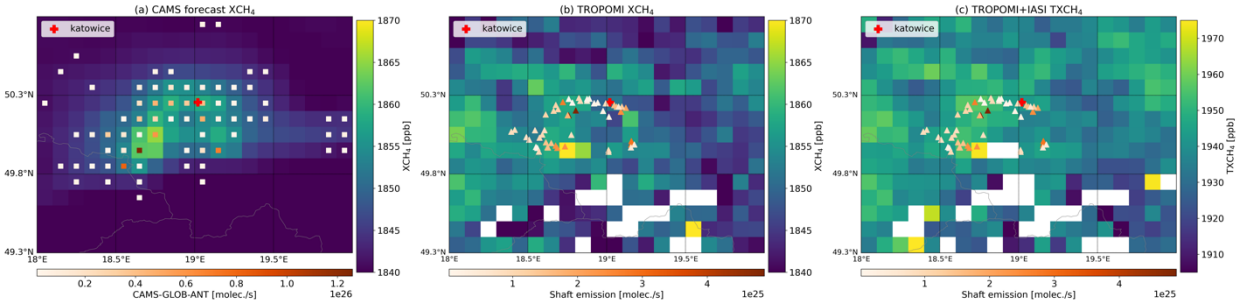

Figure 4: Averaged (a) CAMS forecast XCH_4, (b) TROPOMI XCH_4, and (c) TROPOMI+IASI $TXCH_4$ in the USCB region on a 0.1° × 0.1° latitude/longitude grid during November 2017-December 2020. The square and triangle symbols represent the locations of CAMS-GLOB-ANT sources (for better viewing, only the emission strengths larger than 1E24 molec./s are shown here) and the active coal mine shafts from the CoMet inventory (Gałkowski et al., 2021), respectively. Different colors denote the amount of emission rates. The white grids represent no data from TROPOMI or the number of the points in the grid less than 5. A zoom version of panel (b) is shown in the appendix (Figure A- 2). Note, a different colorbar has been used in panel (c).

Based on the CAMS emissions, the wind-assigned method is applied to CAMS XCH_4. The XCH_4 enhancement (raw-background) and the wind-assigned anomalies are presented in Figure 5a and b, respectively. Note, that the CAMS XCH_4 is coincided with TROPOMI XCH_4 for better comparison. Some data are thus missing here mostly due to the quality filter of TROPOMI observations. After removing the XCH_4 background, the XCH_4 anomalies well represent the CAMS sources. The highest CH_4 sources from the CAMS-GLOB-ANT inventory are also obviously visible in the 2D anomalies. In addition, the spatial distributions of the three XCH_4 data products show different patterns (Figure 4), whereas the anomalies (after removing background) patterns are similar (Figure 5(a) and (d), Figure 7(a) and (d)). This indicates that the background removal is of importance for XCH_4 and our method works well.

The wind-assigned anomalies for CAMS and cone plume model show a very good agreement with a slope of 1.11 and a R^2 of 0.85 (Figure 5c). Our results are derived from the CAMS emission information, and they agree very good with the CAMS model data. The estimated emission rate is about 815 ± 13 kt/year (9.7E26 ± 1.5E25 molec./s) when using the ERA5 wind at 975 hPa (~330 m) and this value is quite close to the CAMS-GLOB-ANT (estimated emission rate at other levels are presented in Sec. 3.2, see Figure 8 as well). Therefore, we use ERA5 wind at this level in the following. Note that the points whose distances to the nearest dominant sources are less than 10 km, are removed here, because they are very close to the significant sources and small changes in wind (either speed or direction) can result in high uncertainties.

The retrieved CH_4 from satellite observations are based on total columns and therefore, these are strongly affected by the stratospheric abundance, i.e., by the changing tropopause altitude (Liu et al., 2021; Schneider et al., 2021). The model simulation uncertainties in representing XCH_4 in the stratosphere might introduce biases in investigating CH_4 sources and sinks (Pandey et al., 2016). To remove this influence, we calculate the tropospheric CAMS forecast CH_4 ($TXCH_4$) from the surface up to 7 km. The results are presented in Figure 5d-f. The CAMS $TXCH_4$ anomalies have similar distribution as CAMS XCH_4, showing that removing the background also works for the tropospheric CH_4. The wind-assigned plume and the correlation between CAMS and the wind-assigned model results are very similar between XCH_4 and $TXCH_4$. The estimated CH_4 emission strength derived from CAMS $TXCH_4$ is 798 ± 11 kt/year (9.5E26 ± 1.3E24 molec./s).

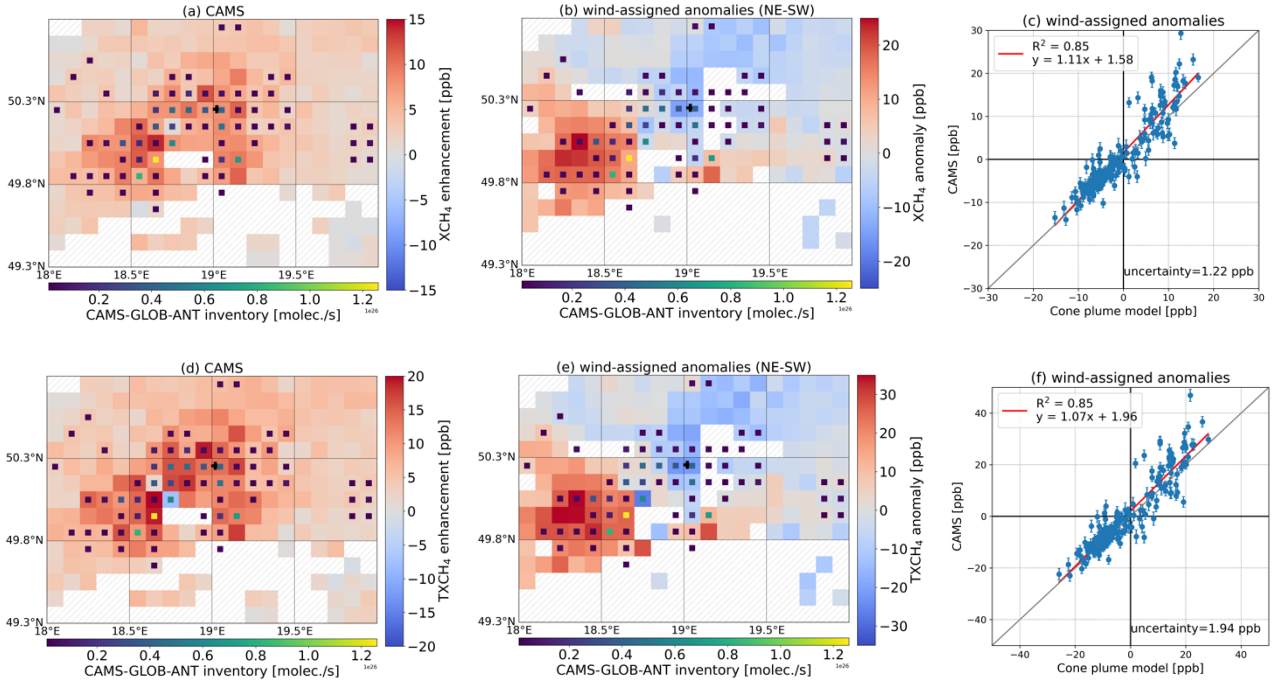

Figure 5: (a)-(c): CAMS XCH_4 enhancement (XCH_4-background), the wind-assigned anomalies (NE-SW), and correlation plot of the wind-assigned anomalies between CAMS and the cone plume model with using the CAMS-GLOB-ANT inventory (9.7E26 molec./s in total) and ERA5 wind at 330 m during November 2017-December 2020 over the USCB region. (d)-(f): the same as for the upper panel but for CAMS $TXCH_4$ (colorbars in (d) and (e) are different from that for XCH_4). The square symbols represent the locations of the CAMS-GLOB-ANT (>1E24 molec./s) inventory and different colors denote the amount of emission rates. The hatched areas in (a)-(b) and (d)-(e) represent no data in these grids. The uncertainties in (c) and (f) represent the mean error bars, i.e., error propagation of the background uncertainty and the CAMS standard deviation.

3.2 Estimated emissions derived from satellite observations

The high-resolution TROPOMI XCH_4 provides the ability to detect and quantify the CH_4 emissions (e.g., oil and gas sector, coal mining) on fine and large scales (Pandey et al., 2019; Varon et al., 2019; Gouw et al., 2020; Schneising et al., 2020). Figure 6 illustrates the enhanced XCH_4 (raw XCH_4-background in the upwind) distribution over the USCB region on an example day (6 June 2018), in which the wind mostly came from northeast. As expected, obvious XCH_4 enhancements were observed by TROPOMI along the downwind direction (southwest of Katowice where most ventilation shafts are located), as well as simulated by the CAMS forecast. The downwind-enhanced XCH_4 modeled by our simple plume model and based on the CAMS-GLOB-ANT inventory also shows a similar shape of plume. This enhancement was also observed by portable FTIR instruments (COCCON) employed during the CoMet campaign (Figure 4 in Luther et al., 2019). The observations support the statement that TROPOMI is able to detect the CH_4 emission signals. In addition, the spatial pattern of the downwind plume is similar to that of the cone-shaped plume, which implies our cone-shape assumption is reasonable.

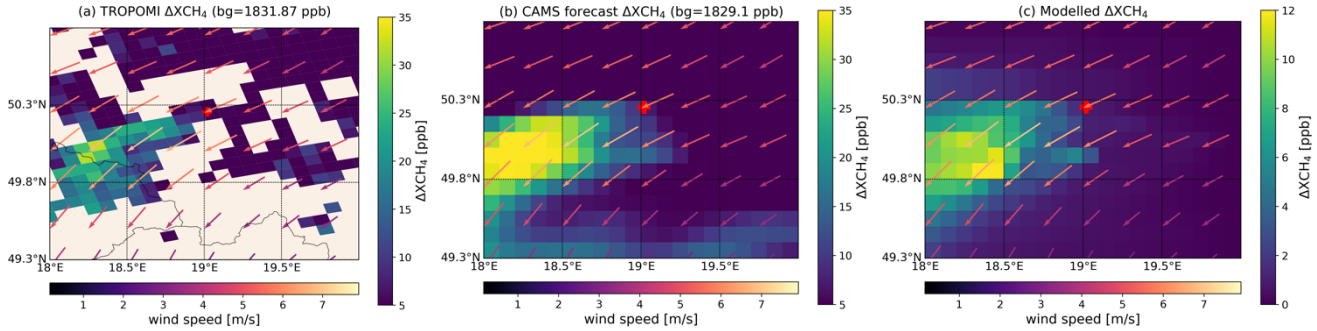

Figure 6: ΔXCH_4 together with the ERA5 wind at 12:00 UTC from (a): TROPOMI observations at 11:34 UTC, (b): CAMS forecast at 12:00 UTC, and (c): from the simple plume model (averaged over the daytime) based on the CAMS-GLOB-ANT inventory over the USCB region on an example day (6 June 2018). The "bg" in the title of (a) and (b) represents the average background, derived from the mean XCH_4 in the upwind region (50.3º-50.8º N, 19.5º -20.0º E).

The three-year averaged TROPOMI XCH_4 observations presented in Figure 4b shows scattered high XCH_4 amounts, whereas CAMS XCH_4 is more concentrated on the center of the study area, and those agree well with its anthropogenic emission sources (CAMS-GLOB-ANT inventory). This might be because TROPOMI detects other real CH_4 sources that are not included in the CAMS forecast model data.

For better comparison with other studies discussing the coal mine emissions in the USCB region, we apply the CoMet inventory as the a priori known sources in the wind-assigned method to estimate the CH_4 emissions. The results are illustrated in Figure 7. The TROPOMI XCH_4 and TROPOMI+IASI $TXCH_4$ anomalies show high concentrations around the areas where the ventilation shafts are located and the region in the northeast of Katowice. Although the anomalies of the satellite observations are lower than the CAMS results (Figure 5a), their spatial distributions are similar. Positive and negative plumes can be clearly seen in Figure 7b and e. The correlation of the wind-assigned anomalies between the TROPOMI and cone plume model has a very good agreement with an R^2 value of 0.76. Similar results are also derived from TROPOMI+IASI $TXCH_4$ with a R^2 value of 0.62. Compared to CAMS data, higher scatter is expected, because satellite observations suffer from observational errors and might contain more CH_4 sources (e.g., landfills, gas distribution network). Although none of these sources have the same orders of magnitude of coal mining emission, they might still bring some errors.

The estimated CH_4 emission strengths are 479 ± 4 kt/year (5.7E26 ± 4.9E24 molec./s) for XCH_4 and 437 ± 18 kt/year (5.2E26 ± 2.2E25 molec./s) for $TXCH_4$, and both are close to the E-PRTR inventory (448 kt/year). The TROPOMI+IASI result has a higher uncertainty than the TROPOMI result, because (1) the vertical distribution of CH_4 is in general much more difficult to measure than the total column of CH_4 and (2) the vertical distribution is derived by considering two independent measurements, each with its own noise error. This might change for a larger number of data points (e.g., by using data from more years or by applying the method to IASI and TROPOMI successors on the upcoming METOP-SG satellite, which offers much more collocated observations).

However, in our study using $TXCH_4$ data in addition to XCH_4 data nicely documents the robustness of the method. Important for a correct estimation of the emission is the correct removal of the methane background signal. For XCH_4 the stratospheric

and the tropospheric backgrounds have to be removed, whereas only the tropospheric background has to be removed for $TXCH_4$. Despite this difference, we estimate very similar emission rates from both data sets and the emission rate uncertainties of using XCH_4 or $TXCH_4$ are small compared to the estimated emission rates.

Figure 8 summarizes the estimated emission strengths derived from different products based on different a priori knowledge of inventories and wind information at different altitudes (for specific values see Table A- 1). Different a priori inventories result in 16%-32% changes in strength at different altitudes, which is generally smaller than the 47% difference in the total amount of inventories (9.7E26 for CAMS-GLOB-ANT and 6.6E26 molec./s for CoMet inventory). This is probably due to the different locations of sources and different proportions of each emission source in the total strengths in the two inventories. When using the CAMS-GLOB-ANT inventory, CH_4 emission rates derived from CAMS XCH_4 and $TXCH_4$ are ~37% and ~56% higher than those derived from TROPOMI XCH_4 and IASI+TROPOMI $TXCH_4$, respectively. This difference is mainly due to the difference between the CAMS forecast and satellite products. The strength increases with respect to the increasing wind speed at higher altitude. Whereas the increment is not always proportional to the wind speed, i.e., less increase in the strength with respect to the wind speed at higher altitude (see Sect. 3.3.1).

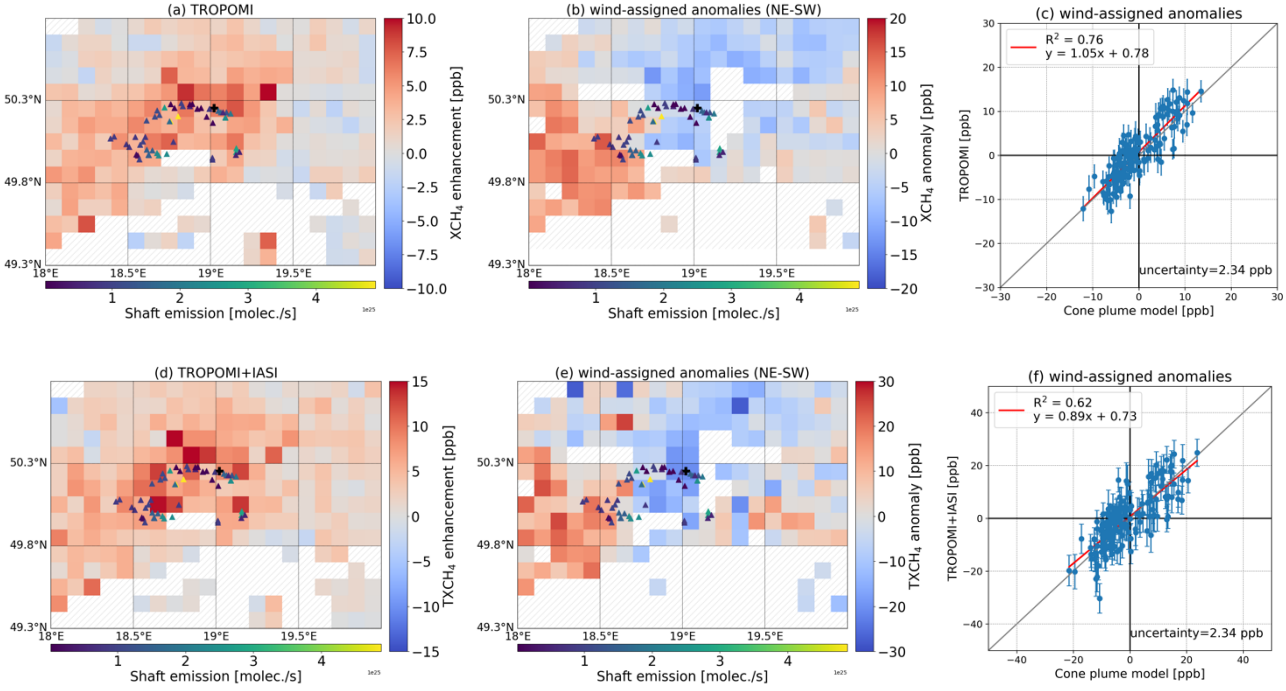

Figure 7: Similar to Figure 5, but for (a-c) TROPOMI XCH_4 and (d-f) TROPOMI+IASI $TXCH_4$. The a priori knowledge of sources are based on the CoMet inventory (6.6E26 molec./s in total, Gałkowski et al., 2021). The triangle symbols represent the locations of the active coal mine shafts and different colors denote the amount of emission rates.

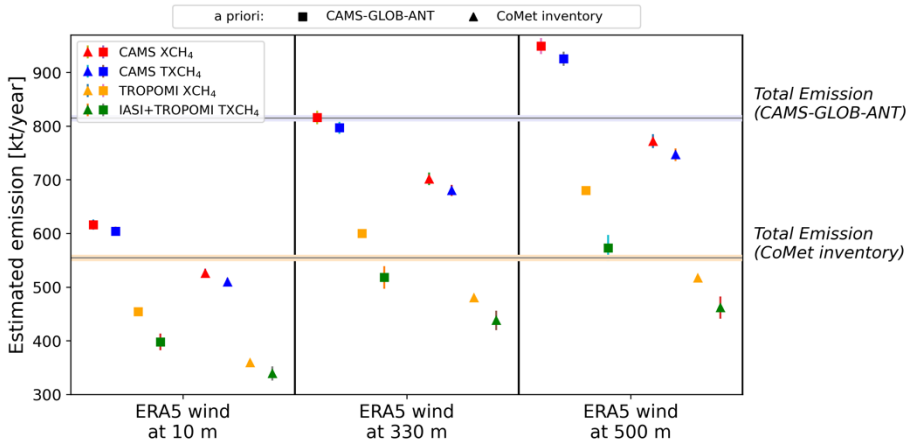

Figure 8: Estimated CH_4 emission rates derived from the CAMS forecasts (XCH_4 and $TXCH_4$), TROPOMI XCH_4, and TROPOMI+IASI $TXCH_4$ data based on different a priori knowledge of emission sources (CAMS-GLOB-ANT and CoMet inventories) and on ERA5 model winds at different altitudes (10 m, 330 m, 500 m). Square symbols represent the a priori emission sources from the CAMS-GLOB-ANT inventory and triangle symbols represent the a priori emission sources from the CoMet inventory. The two horizontal lines represent the number of total emissions for the CAMS-GLOB-ANT inventory (lavender color) and for the CoMet inventory (orange color), respectively. Note, the error bars are much smaller than the results and they are not visible here. For specific values see Table A- 1.

3.3 Uncertainty analysis

CH_4 signal is weak compared to the background concentration which shows an increasing trend with obvious seasonality and strong day-to-day signals. It is necessary to remove the background signals before estimating the emission strengths. However, the imperfect elimination of the background introduces uncertainties, which can be determined by considering the deficits of the background model and the noise in the background (Tu et al., 2022). In this study, the uncertainties of the estimated strengths include the background uncertainties.

Winds, particularly near the surface, are significantly altered by topography, which yields uncertainties in knowing the transport pathway from emission sources to the measurement location (Chen et al., 2016; Babenhauserheide et al., 2020). Thus, wind is one of the most important factors in correctly estimating the emission rates. Here, we investigate the wind uncertainties based on the CAMS XCH_4 and the CAMS-GLOB-ANT inventory. The wind used in Sect. 3.3.2 and 3.3.3 are from ERA5 at 10 m.

3.3.1 Vertical wind shear

Compared to the wind at 330 m, the distributions of wind directions are similar at lower or higher altitudes (10 m and 500 m) but the wind speed increases with higher altitude (Figure 3). The wind speed at 10 m is 20% weaker than that at 330 m (**Table 1**), which yields a corresponding lower emission estimate of 613 ± 9 kt/year (7.3E26 ± 1.1E25 molec./s, -25%) based on the CAMS XCH_4 and CAMS emission inventory (Figure A- 3a).

Assuming that the height of the Planetary Boundary Layer (PBL) is typically less than a kilometer, we use the ERA5 wind at 500 m above the ground (Figure 3c) for describing the transport of methane released in the study region. The wind speed at 500 m increases by 22% and 37% for NE and SW regimes, respectively, i.e., 32% on average, compared to the wind at 330 m. The share of SW directed winds is slightly larger at the 500 m level. These differences result in an increase of 13% of the estimated emission rate (924 ± 14 kt/year, 1.1E27 ± 1.7E25 molec./s). The wind speed is linear in the calculation of ε (Eq. 2), but the wind speeds do not all linearly change for each grid and for each time at different levels. This results in unequal changes between the wind speed and the enhanced columns, and later unequal changes in the estimated emission strength. In addition, the simple cone plume model introduces biases, i.e., the enhanced column in the downwind is set to zero when its location is out of the cone angle (60º). Slight changes in the wind directions might result in a huge difference in the enhanced columns.

3.3.2 Use of narrowed angular wind regimes

The long-term wind comes from all directions (0°-360°) (Figure 3). To define the uncertainty of wind regimes' coverage, the wind is separated into two groups with narrow coverage fields: $NE_{1/2}$ (0°-90°) – $SW_{1/2}$ (180°-270°) and $NW_{1/2}$ (270°-360°) – $SE_{1/2}$ (90°-180°). The final estimated emission strength is weighted by the number of days on which, on average, the wind blew in the respective wind regime (i.e., 115 days for $NE_{1/2}$ – $SW_{1/2}$ and 71 days for $NW_{1/2}$ – $SE_{1/2}$, respectively). The XCH_4 anomalies and the plume for the $NE_{1/2}$ – $SW_{1/2}$ regime are quite similar to those with using wider-coverage NE and SW fields (Figure 9a-c). The wind-assigned anomalies derived from CAMS and the cone plume model show very good agreement as well. Slightly less data points are found here because of the choice of narrower wind fields, especially for $NW_{1/2}$ – $SE_{1/2}$ wind fields. The estimated emission rate is about 773 ± 13 kt/year (9.2E26 ± 1.6E25 molec./s) for the $NE_{1/2}$ – $SW_{1/2}$ field. This indicates that the effect of the segment in the wind field coverage is negligible when there are enough measurements. The use of $NW_{1/2}$ – $SE_{1/2}$ wind fields yields an emission strength of 1176 ± 109 kt/year (1.4E27 ± 1.3E26 molec./s). The higher uncertainty is probably due to less measurements in these wind fields. The weighted rate is therefore about 927 kt/year (1.1E27 molec./s), 13.4% higher than based on the wider NE-SW wind regime (Sec. 3.1).

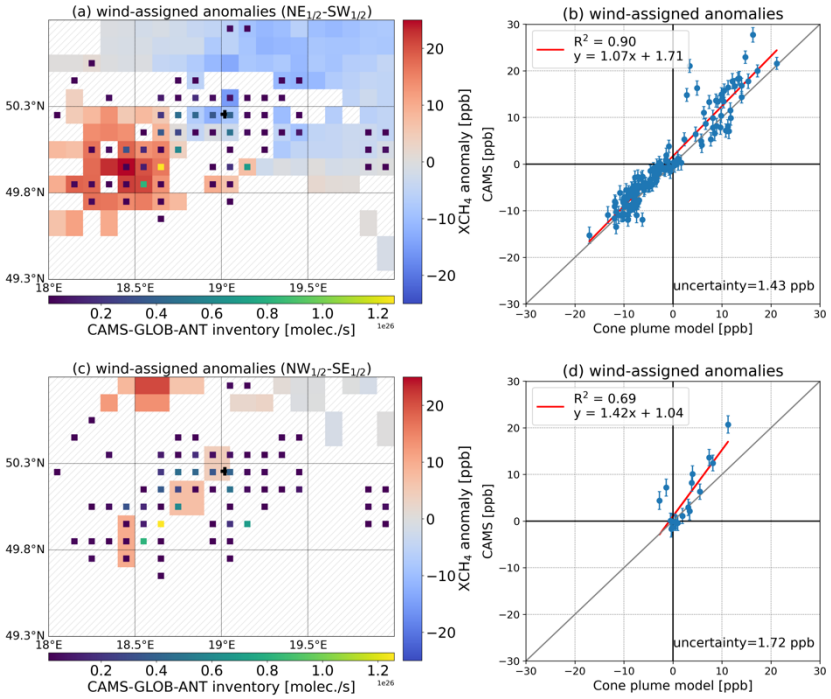

Figure 9: Similar figures to Figure 5b-c. Results are derived from CAMS XCH_4, CAMS emission inventory and ERA5 wind at 330 m for (a)-(b) narrow wind coverage ($NE_{1/2}$ and $SW_{1/2}$), and (c)-(d) narrow wind coverage ($NW_{1/2}$ and $SE_{1/2}$).

3.3.3 Investigation of different choices for wind field segmentation

The wind category here is based on the predominant wind fields over the USCB region and is divided into two opposite regimes (SW and NE). To investigate the effect of the segmentation on the uncertainty in the emission rate estimation, we additionally apply another kind of segmentation: N (<90° or >270°) and S (90° - 270°) categories. Similar results are found and are shown in Figure 10. Though the 2D distribution of the plume changes due to the new wind category, an obvious plume can be seen. The estimated emission rate is 773 ± 15 kt/year (9.2E26 ± 1.8E25 molec./s), which is only 5.2% less than that using NE and SW wind categories. The correlation of the wind-assigned anomalies derived from the CAMS and the cone plume model shows a very good agreement as well, with a similar R^2 value of 0.85 to that in the NE-SW wind category. This result demonstrates that our method is not significantly influenced by the wind regime division.

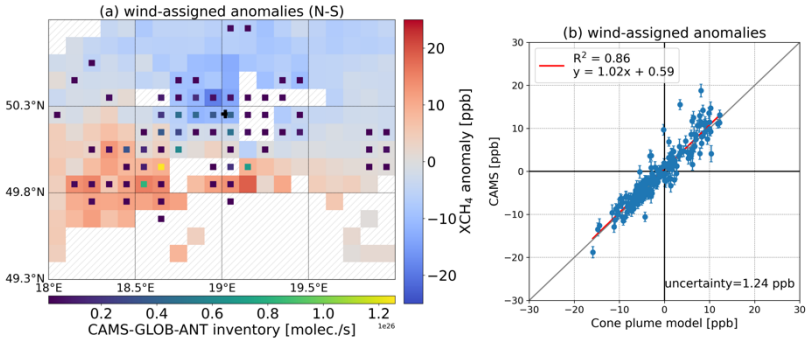

Figure 10: Similar figures to Figure 5b-c. Results are derived from CAMS XCH_4, CAMS emission inventory and ERA5 wind at 330 m but using a new wind category (N and S).

4. Conclusion

Intensive mining activities are the dominant CH_4 emission sources in the USCB region, Poland, where one of the largest coal mining areas in Europe is located. It is thus of importance to quantify the CH_4 emissions from this area. In this study we use the combination of a simple plume model and a novel wind-assigned model to estimate CH_4 emission rates from high-resolution CAMS forecast XCH_4 and $TXCH_4$, along with satellite data (TROPOMI XCH_4 and TROPOMI+IASI $TXCH_4$) over the USCB region (49.3°N-50.8°N and 18°E-20°E) from November 2017 to December 2020.

Based on the CAMS-GLOB-ANT inventory, the dominant CH_4 source is emitted from energy production and distribution, and the significant sources are spread around the city of Katowice and its southwest region. We firstly apply the wind-assigned method to the CAMS forecasts based on the a priori knowledge of CAMS-GLOB-ANT inventory (815 kt/year, 9.7E26 molec./s in total) and ERA5 wind at ~330 m. We use the wind-assigned anomalies of XCH_4/$TXCH_4$ to represent the difference of XCH_4/$TXCH_4$ between the conditions of two opposite wind fields (NE and SW). The wind-assigned anomalies derived from CAMS XCH_4/$TXCH_4$ show very good agreements with the output of the cone plume model with an R^2 value of 0.85 for CAMS XCH_4 and CAMS $TXCH_4$. This nice correlation indicates that our background removal works well. In addition, similar estimates are derived from CAMS XCH_4 (815 ± 13 kt/year, 9.7E26 ± 1.5E25 molec./s) and $TXCH_4$ (798 ± 11 kt/year, 9.5E26 ± 1.3E24 molec./s).

To investigate the CH_4 emissions from this hot spot, the CoMet campaign was performed in 2018. Locations and emission rates of the ventilation shafts of the coal mine used in this study are based on this campaign. Based on this knowledge, the emissions are estimated as 479 ± 4 kt/year (5.7E26 ± 4.9E24 molec./s) and 437 ± 18 kt/year (5.2E26 ± 2.2E25 molec./s) from the TROPOMI XCH_4 and combined TROPOMI+IASI $TXCH_4$, respectively. These results are 40% less than that derived from the CAMS model and CAMS-GLOB-ANT inventory. It is probably because the CAMS-GLOB-ANT includes many sectors of anthropogenic sources, like wastes, and combustion from residential and commercial, which account for about 20%. Nevertheless, our results derived from satellite observations are close to the E-PRTR inventory of 448 kt/year and reasonably

compared to the CoMet inventory (555 kt/year), and to previous studies over the USCB region (ranging from 9 kt/year to 79 kt/year for a sub-cluster of shafts (Krautwurst et al., 2021) up to 477 kt/year derived from one flight (Fiehn et al. (2021)).

Similar 2D anomalies and plumes are also observed for TROPOMI XCH_4 and TROPOMI+IASI $TXCH_4$. This nicely documents the robustness of the method. The TROPOMI+IASI result has a higher uncertainty than the TROPOMI result, because (1) the vertical distribution of CH_4 is in general much more difficult to measure than the total column of CH_4 and (2) the vertical distribution is derived by considering two independent measurements, each with its own noise error. This might change for a larger number of data points (e.g., by using data from more years or by applying the method to IASI and TROPOMI successors on the upcoming METOP-SG satellite, which offers much more collocated observations). Nonetheless, the uncertainties are insignificant compared to the estimated emission rates.

Wind contains uncertainties in knowing the transport pathway from emission sources to the measurement location and thus, we analyze the effects in selecting wind at lower and higher altitude (10 m and 500 m), wind field coverage and wind category. Wind distributions at higher levels are similar to the ones at 330 m. However, their speeds decrease by 20% at 10 m and increase by 32% at 500 m, which results in changes in the emission rates by -25% and 13 %, respectively. Narrower wind field coverage (0°-90° for NE regime and 180°-270° for SW regime) and different wind segmentation (<90° or >270° for N regime and 90°-270° for S regime) introduce uncertainties of +13.4% and -5.2%, respectively. The agreements for these sensitivity tests of the wind-assigned anomalies derived from the CAMS and from the cone plume model are as good as that using previous NE and SW wind fields. The results suggest that our method is robust since it is insensitive to the separation of the wind regimes. It is also suitable for estimating CH_4 and CO_2 emissions in other regions.

Data availability. The data are accessible by contacting the corresponding author (qiansi.tu@kit.edu). The SRON S5P-RemoTeC scientific TROPOMI CH_4 dataset from this study is available for download at https://doi.org/10.5281/zenodo.4447228 (Lorente et al., 2021, last access: 08 November 2021). The TROPOMI data set is publicly available from https://scihub.copernicus.eu/ (last access: 08 November 2021; ESA, 2020). The access and use of any Copernicus Sentinel data available through the Copernicus Open Access Hub are governed by the legal notice on the use of Copernicus Sentinel Data and Service Information, which is given here: https://sentinels.copernicus.eu/documents/247904/690755/Sentinel_Data_Legal_Notice (last access: 08 November 2021; European Commission, 2020). The MUSICA IASI data set is available for download via https://doi.org/10.35097/408 (Schneider et al. 2021).

Author contributions. Qiansi Tu, Frank Hase and Matthias Schneider developed the research question. Qiansi Tu wrote the manuscript and performed the data analysis with input from Frank Hase, Matthias Schneider and Farahnaz Khosrawi. Matthias Schneider, Benjamin Ertl and Christopher J. Diekmann provided the combined (MUSICA IASI + TROPOMI) data and supported technically for the analysis of these data. Jarosław Necki supported in consultation of the local situation and CoMet inventory. All authors discussed the results and contributed to the final manuscript.

Competing interests. The authors declare that they have no conflict of interest.

Acknowledgements. The CAMS results were generated using Copernicus Atmosphere Monitoring Service (2017–2020) information. Neither the European Commission nor ECMWF is responsible for any use that may be made of the Copernicus information or data it contains. We also thank Michela Giusti and Kevin Marsh in the Data Support Team at ECMWF for retrieving and providing comments about the CAMS data. This research has largely benefit from funds of the Deutsche Forschungsgemeinschaft (provided for the two projects MOTIV and TEDDY with IDs/290612604 and 416767181, respectively). Important part of this work was performed on the supercomputer ForHLR funded by the Ministry of Science, Research and the Arts Baden-Württemberg and by the German Federal Ministry of Education and Research. We acknowledge Emissions of atmospheric Compounds and Compilation of Ancillary Data (ECCAD) for providing CAMS-GLOB-ANT inventory data. We also give thanks to Claire Granier from Laboratoire d'Aerologie, Toulouse, France for providing information about the uncertainties of the CAMS-GLOB-ANT inventory.

We acknowledge the support by the Deutsche Forschungsgemeinschaft and the Open Access Publishing Fund of the Karlsruhe Institute of Technology.

Appendix

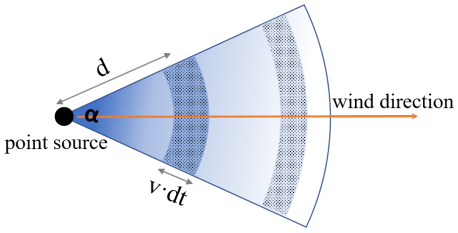

Figure A- 1: Sketch of the simple plume model used to explain the CH_4 emission estimation method. The methane at the point source is distributed along the wind direction (wind speed: v) in the cone-shaped area with an opening angle of α. The point source emits the methane at an emission rate of ε. We assumed the methane molecules are evenly distributed in the dotted area A, and the distance from area A to the point source is d. Therefore, the emitted methane in dt time period equals to the amount of methane in the area A. It yields the equation $\varepsilon \times dt \approx \Delta column \times \frac{\alpha}{\pi} \times \pi \times d \times v \times dt$. This figure is adopted from Tu et al. (2022).

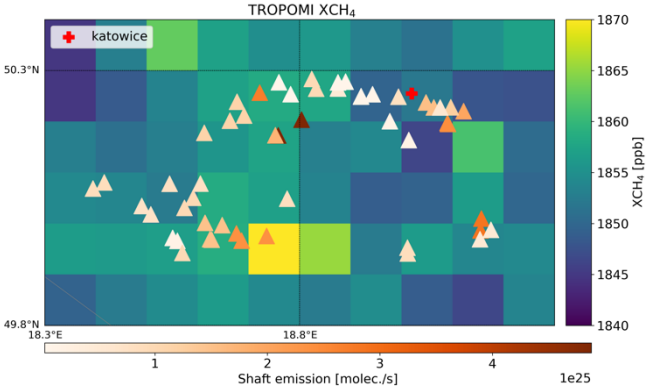

Figure A- 2: A zoomed figure of Figure 4(b).

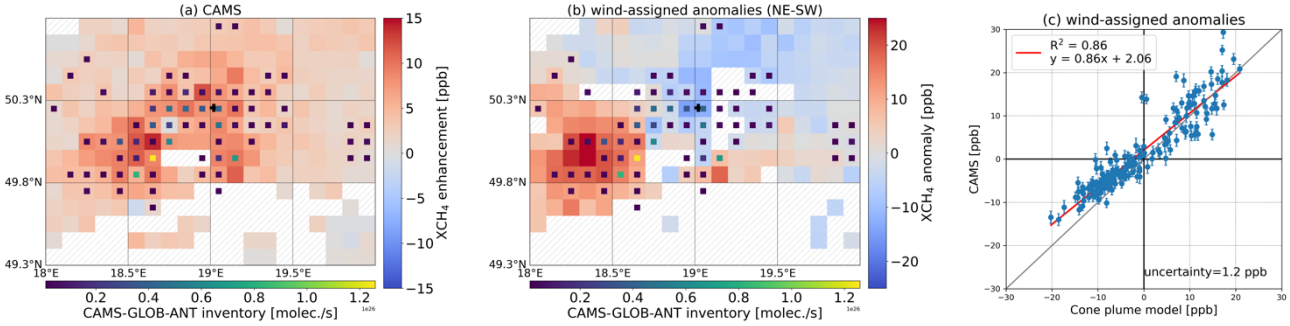

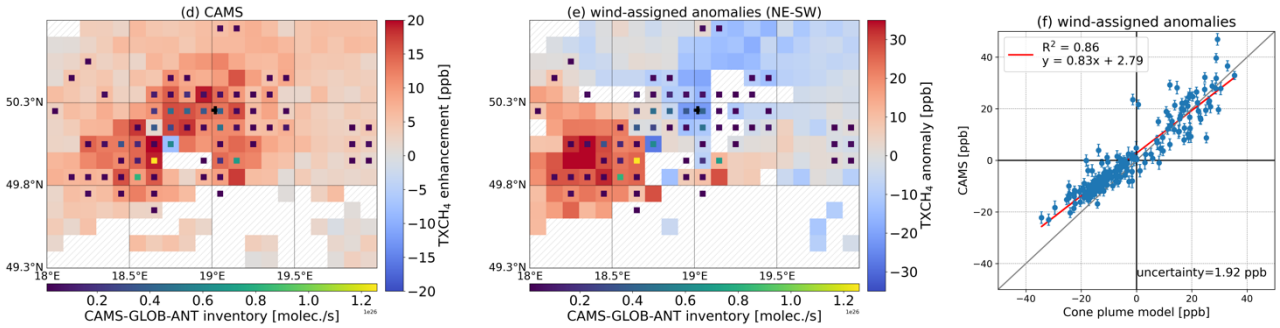

Figure A- 3: Similar to Figure 5 but using ERA5 wind at 10 m.

460

Table A- 1: Estimated CH_4 emission rates derived from CAMS forecasts (XCH_4 and $TXCH_4$), TROPOMI XCH_4, and IASI&TROPOMI $TXCH_4$ data based on different a priori knowledge of emission sources (CAMS-GLOB-ANT and CoMet campaign inventories) and ERA5 model winds at different altitudes (10 m, 100 m and ~500 m).

	ERA5 wind at 10 m		ERA5 wind at 330 m (975 hPa)		ERA5 wind at 500 m (950 hPa)	
prior emission sources	CAMS-GLOB-ANT (total = 9.7E26 molec./s)	CoMet inventory (total = 6.6E26 molec./s)	CAMS-GLOB-ANT (total = 9.7E26 molec./s)	CoMet inventory (total = 6.6E26 molec./s)	CAMS-GLOB-ANT (total = 9.7E26 molec./s)	CoMet inventory (total = 6.6E26 molec./s)
CAMS XCH_4	7.3E26 ± 1.1E25	6.3E26 ± 1.0E25	9.7E26 ± 1.5E25	8.3E26 ± 1.4E25	1.1E27 ± 1.8E25	9.2E26 ± 1.6E25
CAMS $TXCH_4$	7.2E26 ± 9.4E24	6.1E26 ± 9.1E24	9.5E26 ± 1.3E25	8.1E26 ± 1.4E25	1.0E27 ± 1.6E25	8.9E26 ± 1.4E25
TROPOMI XCH_4	5.4E26 ± 4.8E24	4.5E26 ± 4.1E24	7.1E26 ± 6.4E24	5.9E26 ± 5.6E24	8.1E26 ± 7.5E24	6.3E26 ± 6.2E24
IASI&TROPOMI $TXCH_4$	4.7E26 ± 1.9E25	4.0E26 ± 1.6E25	6.2E24 ± 2.5E25	5.2E26 ± 2.2E25	6.8E24 ± 2.9E25	5.5E26 ± 2.4E25

465

References

Agustí-Panareda, A., Diamantakis, M., Massart, S., Chevallier, F., Muñoz-Sabater, J., Barré, J., Curcoll, R., Engelen, R., Langerock, B., Law, R. M., Loh, Z., Morguí, J. A., Parrington, M., Peuch, V.-H., Ramonet, M., Roehl, C., Vermeulen, A. T., Warneke, T., and Wunch, D.: Modelling CO2 weather – why horizontal resolution matters, Atmos. Chem. Phys., 19, 7347–7376, https://doi.org/10.5194/acp-19-7347-2019, 2019.

Andersen, T., Vinkovic, K., de Vries, M., Kers, B., Necki, J., Swolkien, J., Roiger, A., Peters, W. and Chen, H.: Quantifying methane emissions from coal mining ventilation shafts using an unmanned aerial vehicle (UAV)-based active AirCore system, Atmos. Environ. X, 12, 100135, doi:https://doi.org/10.1016/j.aeaoa.2021.100135, 2021.

Babenhauserheide, A., Hase, F., and Morino, I.: Net CO2 fossil fuel emissions of Tokyo estimated directly from measurements of the Tsukuba TCCON site and radiosondes, Atmos. Meas. Tech., 13, 2697–2710, https://doi.org/10.5194/amt-13-2697-2020, 2020.

Barré, J., Aben, I., Agustí-Panareda, A., Balsamo, G., Bousserez, N., Dueben, P., Engelen, R., Inness, A., Lorente, A., McNorton, J., Peuch, V.-H., Radnoti, G., and Ribas, R.: Systematic detection of local CH4 anomalies by combining satellite measurements with high-resolution forecasts, Atmos. Chem. Phys., 21, 5117–5136, https://doi.org/10.5194/acp-21-5117-2021, 2021.

Boesch, H., Baker, D., Connor, B., Crisp, D. and Miller, C.: Global Characterization of CO2 Column Retrievals from Shortwave-Infrared Satellite Observations of the Orbiting Carbon Observatory-2 Mission, Remote Sens. , 3(2), doi:10.3390/rs3020270, 2011.

Butz, A., Hasekamp, O. P., Frankenberg, C., and Aben, I.: Retrievals of atmospheric CO2 from simulated space-borne measurements of backscattered near-infrared sunlight: accounting for aerosol effects, Appl. Opt. 48, 3322-3336, 2009.

Butz, A., Hasekamp, O. P., Frankenberg, C., Vidot, J. and Aben, I.: CH4 retrievals from space-based solar backscatter measurements: Performance evaluation against simulated aerosol and cirrus loaded scenes, J. Geophys. Res. Atmos., 115(D24), doi:https://doi.org/10.1029/2010JD014514, 2010.

Butz, A., Guerlet, S., Hasekamp, O., Schepers, D., Galli, A., Aben, I., Frankenberg, C., Hartmann, J.-M., Tran, H., Kuze, A., Keppel-Aleks, G., Toon, G., Wunch, D., Wennberg, P., Deutscher, N., Griffith, D., Macatangay, R., Messerschmidt, J., Notholt, J., and Warneke, T.: Toward accurate CO2 and CH4 observations from GOSAT, Geophysical Research Letters, 38, https://doi.org/10.1029/2011GL047888, https://agupubs.onlinelibrary.wiley.com/doi/abs/10.1029/2011GL047888, 2011.

Chen, J., Viatte, C., Hedelius, J. K., Jones, T., Franklin, J. E., Parker, H., Gottlieb, E. W., Wennberg, P. O., Dubey, M. K., and 595 Wofsy, S. C.: Differential column measurements using compact solar-tracking spectrometers, Atmos. Chem. Phys., 16, 8479–8498, https://doi.org/10.5194/acp-16-8479-2016, 2016.

Collard, A. D.: Selection of IASI Channels for Use in Numerical Weather Prediction, ECMWF, https://www.ecmwf.int/node/8760, 2007.

Coopmann, O., Guidard, V., Fourrié, N., Josse, B., and Marécal, V.: Update of Infrared Atmospheric Sounding Interferometer (IASI) channel selection with correlated observation errors for numerical weather prediction (NWP), Atmos. Meas. Tech., 13, 2659–2680, https://doi.org/10.5194/amt-13-2659-2020, 2020.

Copernicus Climate Change Service (C3S): ERA5: Fifth generation of ECMWF atmospheric reanalyses of the global climate. Copernicus Climate Change Service Climate Data Store (CDS), date of access. https://cds.climate.copernicus.eu/cdsapp#!/home, 2017.

Crippa, M., Guizzardi, D., Muntean, M., Schaaf, E., Dentener, F., van Aardenne, J. A., Monni, S., Doering, U., Olivier, J. G. J., Pagliari, V., and Janssens-Maenhout, G.: Gridded emissions of air pollutants for the period 1970–2012 within EDGAR v4.3.2, Earth Syst. Sci. Data, 10, 1987–2013, https://doi.org/10.5194/essd-10-1987-2018, 2018.

Diekmann, C. J., Schneider, M., Ertl, B., Hase, F., García, O., Khosrawi, F., Sepúlveda, E., Knippertz, P., and Braesicke, P.: The global and multi-annual MUSICA IASI {H2O, δD} pair dataset, Earth Syst. Sci. Data, 13, 5273–5292, https://doi.org/10.5194/essd-13-5273-2021, 2021.

Fiehn, A., Kostinek, J., Eckl, M., Klausner, T., Gałkowski, M., Chen, J., Gerbig, C., Röckmann, T., Maazallahi, H., Schmidt, M., Korbeń, P., Nęçki, J., Jagoda, P., Wildmann, N., Mallaun, C., Bun, R., Nickl, A.-L., Jöckel, P., Fix, A., and Roiger, A.: Estimating CH4, CO2 and CO emissions from coal mining and industrial activities in the Upper Silesian Coal Basin using an aircraft-based mass balance approach, Atmos. Chem. Phys., 20, 12675–12695, https://doi.org/10.5194/acp-20-12675-2020, 2020.

Flemming, J., Huijnen, V., Arteta, J., Bechtold, P., Beljaars, A., Blechschmidt, A.-M., Diamantakis, M., Engelen, R. J., Gaudel, A., Inness, A., Jones, L., Josse, B., Katragkou, E., Marecal, V., Peuch, V.-H., Richter, A., Schultz, M. G., Stein, O., and Tsikerdekis, A.: Tropospheric chemistry in the Integrated Forecasting System of ECMWF, Geosci. Model Dev., 8, 975–1003, https://doi.org/10.5194/gmd-8-975-2015, 2015.

De Gouw, J. A., Veefkind, J. P., Roosenbrand, E., Dix, B., Lin, J. C., Landgraf, J., and Levelt, P. F.: Daily Satellite Observations of Methane from Oil and Gas Production Regions in the United States, Scientific Reports, 10, 1379, https://doi.org/10.1038/s41598-020-57678-4, 2020.

Gałkowski, M., Fiehn, A., Swolkien, J., Stanisavljevic, M., Korben, P., Menoud, M., Necki, J., Roiger, A., Röckmann, T., Gerbig, C., & Fix, A. (2021). Emissions of CH4 and CO2 over the Upper Silesian Coal Basin (Poland) and its vicinity (4.01) [Data set]. ICOS ERIC - Carbon Portal. https://doi.org/10.18160/3K6Z-4H73.

García, O. E., Schneider, M., Ertl, B., Sepúlveda, E., Borger, C., Diekmann, C., Wiegele, A., Hase, F., Barthlott, S., Blumenstock, T., Raffalski, U., Gómez-Peláez, A., Steinbacher, M., Ries, L., and de Frutos, A. M.: The MUSICA IASI CH4 and N2O products and their comparison to HIPPO, GAW and NDACC FTIR references, Atmos. Meas. Tech., 11, 4171–4215, https://doi.org/10.5194/amt-11-4171-2018, 2018.

Granier, C., S. Darras, H. Denier van der Gon, J. Doubalova, N. Elguindi, B. Galle, M. Gauss, M. Guevara, J.-P. Jalkanen, J. Kuenen, C. Liousse, B. Quack, D. Simpson, K. Sindelarova, The Copernicus Atmosphere Monitoring Service global and regional emissions (April 2019 version), Copernicus Atmosphere Monitoring Service (CAMS) report, doi:10.24380/d0bn-kx16, 2019.

Hasekamp, O. P., and Butz, A.: Efficient calculation of intensity and polarization spectra in vertically inhomogeneous scattering and absorbing atmospheres, J. Geophys. Res., 113, D20309, doi:10.1029/2008JD010379, 2008.

Hasekamp, O., Lorente, A., Hu, H., Butz, A., aan de Brugh, J., and Landgraf, J.: Algorithm Theoretical Baseline Document for Sentinel-5 Precursor methane retrieval, http://www.tropomi.eu/documents/atbd/, 2019.

Hersbach, H., Bell, B., Berrisford, P., Hirahara, S., Horányi, A., Muñoz-Sabater, J., Nicolas, J., Peubey, C., Radu, R., Schepers, D., Simmons, A., Soci, C., Abdalla, S., Abellan, X., Balsamo, G., Bechtold, P., Biavati, G., Bidlot, J., Bonavita, M., De Chiara, G., Dahlgren, P., Dee, D., Diamantakis, M., Dragani, R., Flemming, J., Forbes, R., Fuentes, M., Geer, A., Haimberger, L., Healy, S., Hogan, R. J., Hólm, E., Janisková, M., Keeley, S., Laloyaux, P., Lopez, P., Lupu, C., Radnoti, G., de Rosnay, P., Rozum, I., Vamborg, F., Villaume, S. and Thépaut, J.-N.: The ERA5 global reanalysis, Q. J. R. Meteorol. Soc., 146(730), 1999–2049, doi:https://doi.org/10.1002/qj.3803, 2020.

Hoesly, R. M., Smith, S. J., Feng, L., Klimont, Z., Janssens-Maenhout, G., Pitkanen, T., Seibert, J. J., Vu, L., Andres, R. J., Bolt, R. M., Bond, T. C., Dawidowski, L., Kholod, N., Kurokawa, J.-I., Li, M., Liu, L., Lu, Z., Moura, M. C. P., O'Rourke, P. R., and Zhang, Q.: Historical (1750–2014) anthropogenic emissions of reactive gases and aerosols from the Community Emissions Data System (CEDS), Geosci. Model Dev., 11, 369–408, https://doi.org/10.5194/gmd-11-369-2018, 2018.

Kirschke, S., Bousquet, P., Ciais, P., Saunois, M., Canadell, J. G., Dlugokencky, E. J., Bergamaschi, P., Bergmann, D., Blake, D. R., Bruhwiler, L., Cameron-Smith, P., Castaldi, S., Chevallier, F., Feng, L., Fraser, A., Heimann, M., Hodson, E. L., Houweling, S., Josse, B., Fraser, P. J., Krummel, P. B., Lamarque, J.-F., Langenfelds, R. L., Le Quéré, C., Naik, V., O'Doherty, S., Palmer, P. I., Pison, I., Plummer, D., Poulter, B., Prinn, R. G., Rigby, M., Ringeval, B., Santini, M., Schmidt, M., Shindell, D. T., Simpson, I. J., Spahni, R., Steele, L. P., Strode, S. A., Sudo, K., Szopa, S., van der Werf, G. R., Voulgarakis, A., van Weele, M., Weiss, R. F., Williams, J. E. and Zeng, G.: Three decades of global methane sources and sinks, Nat. Geosci., 6(10), 813–823, doi:10.1038/ngeo1955, 2013.

Kostinek, J., Roiger, A., Eckl, M., Fiehn, A., Luther, A., Wildmann, N., Klausner, T., Fix, A., Knote, C., Stohl, A., and Butz, A.: Estimating Upper Silesian coal mine methane emissions from airborne in situ observations and dispersion modeling, Atmos. Chem. Phys., 21, 8791–8807, https://doi.org/10.5194/acp-21-8791-2021, 2021.

Krautwurst, S., Gerilowski, K., Borchardt, J., Wildmann, N., Gałkowski, M., Swolkień, J., Marshall, J., Fiehn, A., Roiger, A., Ruhtz, T., Gerbig, C., Necki, J., Burrows, J. P., Fix, A., and Bovensmann, H.: Quantification of CH_4 coal mining emissions in Upper Silesia by passive airborne remote sensing observations with the Methane Airborne MAPper (MAMAP) instrument during the CO_2 and Methane (CoMet) campaign, Atmos. Chem. Phys., 21, 17345–17371, https://doi.org/10.5194/acp-21-17345-2021, 2021.

Landgraf, J., Butz, A., Hasekamp, O., Hu, H., and aan de Brugh, J.: Sentinel 5 L2 Prototype Processors, Algorithm Theoretical Baseline Document: Methane Retrieval, 2019.

Liu, M., van der A, R., van Weele, M., Eskes, H., Lu, X., Veefkind, P., de Laat, J., Kong, H., Wang, J., Sun, J., Ding, J., Zhao, Y. and Weng, H.: A New Divergence Method to Quantify Methane Emissions Using Observations of Sentinel-5P TROPOMI, Geophys. Res. Lett., 48(18), e2021GL094151, doi:https://doi.org/10.1029/2021GL094151, 2021.

Lorente, A., Borsdorff, T., Butz, A., Hasekamp, O., aan de Brugh, J., Schneider, A., Wu, L., Hase, F., Kivi, R., Wunch, D., Pollard, D. F., Shiomi, K., Deutscher, N. M., Velazco, V. A., Roehl, C. M., Wennberg, P. O., Warneke, T., and Landgraf, J.: Methane retrieved from TROPOMI: improvement of the data product and validation of the first 2 years of measurements, Atmos. Meas. Tech., 14, 665–684, https://doi.org/10.5194/amt-14-665-2021, 2021.

Luther, A., Kleinschek, R., Scheidweiler, L., Defratyka, S., Stanisavljevic, M., Forstmaier, A., Dandocsi, A., Wolff, S., Dubravica, D., Wildmann, N., Kostinek, J., Jöckel, P., Nickl, A.-L., Klausner, T., Hase, F., Frey, M., Chen, J., Dietrich, F., Nęcki, J., Swolkień, J., Fix, A., Roiger, A., and Butz, A.: Quantifying $C4_4$ emissions from hard coal mines using mobile sun-viewing Fourier transform spectrometry, Atmos. Meas. Tech., 12, 5217–5230, https://doi.org/10.5194/amt-12-5217-2019, 2019.

Luther, A., Kostinek, J., Kleinschek, R., Defratyka, S., Stanisavljevic, M., Forstmaier, A., Dandocsi, A., Scheidweiler, L., Dubravica, D., Wildmann, N., Hase, F., Frey, M. M., Chen, J., Dietrich, F., Necki, J., Swolkien, J., Knote, C., Vardag, S. N., Roiger, A., and Butz, A.: Observational constraints on methane emissions from Polish coal mines using a ground-based remote sensing network, Atmos. Chem. Phys. Discuss. [preprint], https://doi.org/10.5194/acp-2021-978, in review, 2021.

Pandey, S., Houweling, S., Krol, M., Aben, I., Chevallier, F., Dlugokencky, E. J., Gatti, L. V., Gloor, E., Miller, J. B., Detmers, R., Machida, T., and Röckmann, T.: Inverse modeling of GOSAT-retrieved ratios of total column CH4 and CO2 for 2009 and 2010, Atmos. Chem. Phys., 16, 5043–5062, https://doi.org/10.5194/acp-16-5043-2016, 2016.

Pandey, S., Gautam, R., Houweling, S., van der Gon, H. D., Sadavarte, P., Borsdorff, T., Hasekamp, O., Landgraf, J., Tol, P., van Kempen, T., Hoogeveen, R., van Hees, R., Hamburg, S. P., Maasakkers, J. D., and Aben, I.: Satellite observations reveal extreme methane leakage from a natural gas well blowout, Proc Natl Acad Sci USA, 116, 26376, https://doi.org/10.1073/pnas.1908712116, 2019.

Prather, M. J., Holmes, C. D. and Hsu, J.: Reactive greenhouse gas scenarios: Systematic exploration of uncertainties and the role of atmospheric chemistry, Geophys. Res. Lett., 39(9), doi:https://doi.org/10.1029/2012GL051440, 2012.

IPCC, 2014: Climate Change 2014: Synthesis Report. Contribution of Working Groups I, II and III to the Fifth Assessment Report of the Intergovernmental Panel on Climate Change [Core Writing Team, R.K. Pachauri and L.A. Meyer (eds.)]. IPCC, Geneva, Switzerland, 151 pp.

Saunois, M., Stavert, A. R., Poulter, B., Bousquet, P., Canadell, J. G., Jackson, R. B., Raymond, P. A., Dlugokencky, E. J., Houweling, S., Patra, P. K., Ciais, P., Arora, V. K., Bastviken, D., Bergamaschi, P., Blake, D. R., Brailsford, G., Bruhwiler, L., Carlson, K. M., Carrol, M., Castaldi, S., Chandra, N., Crevoisier, C., Crill, P. M., Covey, K., Curry, C.

L., Etiope, G., Frankenberg, C., Gedney, N., Hegglin, M. I., Höglund-Isaksson, L., Hugelius, G., Ishizawa, M., Ito, A., Janssens-Maenhout, G., Jensen, K. M., Joos, F., Kleinen, T., Krummel, P. B., Langenfelds, R. L., Laruelle, G. G., Liu, L., Machida, T., Maksyutov, S., McDonald, K. C., McNorton, J., Miller, P. A., Melton, J. R., Morino, I., Müller, J., Murguia-Flores, F., Naik, V., Niwa, Y., Noce, S., O'Doherty, S., Parker, R. J., Peng, C., Peng, S., Peters, G. P., Prigent, C., Prinn, R., Ramonet, M., Regnier, P., Riley, W. J., Rosentreter, J. A., Segers, A., Simpson, I. J., Shi, H., Smith, S. J., Steele, L. P., Thornton, B. F., Tian, H., Tohjima, Y., Tubiello, F. N., Tsuruta, A., Viovy, N., Voulgarakis, A., Weber, T. S., van Weele, M., van der Werf, G. R., Weiss, R. F., Worthy, D., Wunch, D., Yin, Y., Yoshida, Y., Zhang, W., Zhang, Z., Zhao, Y., Zheng, B., Zhu, Q., Zhu, Q., and Zhuang, Q.: The Global Methane Budget 2000–2017, Earth Syst. Sci. Data, 12, 1561–1623, https://doi.org/10.5194/essd-12-1561-2020, 2020.

Schneider, M., Ertl, B., Diekmann, C. J., Khosrawi, F., Röhling, A. N., Hase, F., Dubravica, D., García, O. E., Sepúlveda, E., Borsdorff, T., Landgraf, J., Lorente, A., Chen, H., Kivi, R., Laemmel, T., Ramonet, M., Crevoisier, C., Pernin, J., Steinbacher, M., Meinhardt, F., Deutscher, N. M., Griffith, D. W. T., Velazco, V. A., and Pollard, D. F.: Synergetic use of IASI and TROPOMI space borne sensors for generating a tropospheric methane profile product, Atmos. Meas. Tech. Discuss. [preprint], https://doi.org/10.5194/amt-2021-31, in review, 2021.

Schneider, M., Ertl, B., Diekmann, C. J., Khosrawi, F., Weber, A., Hase, F., Höpfner, M., García, O. E., Sepúlveda, E., and Kinnison, D.: Design and description of the MUSICA IASI full retrieval product, Earth Syst. Sci. Data, 14, 709–742, https://doi.org/10.5194/essd-14-709-2022, 2022.

Schepers, D., Guerlet, S., Butz, A., Landgraf, J., Frankenberg, C., Hasekamp, O., Blavier, J.-F., Deutscher, N. M., Griffith, D. W. T., Hase, F., Kyro, E., Morino, I., Sherlock, V., Sussmann, R. and Aben, I.: Methane retrievals from Greenhouse Gases Observing Satellite (GOSAT) shortwave infrared measurements: Performance comparison of proxy and physics retrieval algorithms, J. Geophys. Res. Atmos., 117(D10), doi:https://doi.org/10.1029/2012JD017549, 2012.

Schneising, O., Buchwitz, M., Reuter, M., Vanselow, S., Bovensmann, H., and Burrows, J. P.: Remote sensing of methane leakage from natural gas and petroleum systems revisited, Atmos. Chem. Phys., 20, 9169–9182, https://doi.org/10.5194/acp-20-9169-2020, 2020.

Tu, Q., Hase, F., Schneider, M., García, O., Blumenstock, T., Borsdorff, T., Frey, M., Khosrawi, F., Lorente, A., Alberti, C., Bustos, J. J., Butz, A., Carreño, V., Cuevas, E., Curcoll, R., Diekmann, C. J., Dubravica, D., Ertl, B., Estruch, C., León-Luis, S. F., Marrero, C., Morgui, J.-A., Ramos, R., Scharun, C., Schneider, C., Sepúlveda, E., Toledano, C., and Torres, C.: Quantification of CH_4 emissions from waste disposal sites near the city of Madrid using ground- and space-based observations of COCCON, TROPOMI and IASI, Atmos. Chem. Phys., 22, 295–317, https://doi.org/10.5194/acp-22-295-2022, 2022.

Varon, D. J., McKeever, J., Jervis, D., Maasakkers, J. D., Pandey, S., Houweling, S., Aben, I., Scarpelli, T. and Jacob, D. J. : Satellite discovery of anomalously large methane point sources from oil/gas production, Geophysical Research Letters, 46, 13507– 13516. https://doi.org/10.1029/2019GL083798, 2019.

Veefkind, J. P., Aben, I., McMullan, K., Förster, H., de Vries, J., Otter, G., Claas, J., Eskes, H. J., de Haan, J. F., Kleipool, Q., van Weele, M., Hasekamp, O., Hoogeveen, R., Landgraf, J., Snel, R., Tol, P., Ingmann, P., Voors, R., Kruizinga, B., Vink, R., Visser, H., and Levelt, P. F.: TROPOMI on the ESA Sentinel-5 Precursor: A GMES mission for global observations of the atmospheric composition for climate, air quality and ozone layer applications, Remote Sens. Environ., 120, 70–83, https://doi.org/10.1016/j.rse.2011.09.027, 2012.

World Meteorological Organisation, WMO greenhouse gas bulletin No. 16.23 Novembet 2020 [Online]. Available at: https://public.wmo.int/en/resources/library/wmo-greenhouse-gas-bulletin, 2020.